# COMPARISION OF FATIGUE AND FRACTURE BEHAVIOR OF WELDED AND SEAMLESS PIPE STEEL IN GASEOUS HYDROGEN

Milan Agnani[1a], Joseph Ronevich[1b], Mihaela E. Cristea[2], Chris San Marchi[1c]

[1]Sandia National Laboratories California
7011 East Avenue, CA, USA, 94550
Phone: (925) 294 3000
Email: 1a – magnani@sandia.gov, 1b – jaronev@sandia.gov, 1c – cwsanma@sandia.gov

[2]Tenaris-Dalmine
Piazza Caduti 6 Luglio 1944, Dalmine, Bergamo, Italy, 24044
Phone: +39 035 560 111
Email: mcristea@tenaris.com

Keywords: Fatigue, Fracture, Pipeline Steels, Microstructures, Hydrogen Embrittlement, Weld, Heat Affected Zone

## ABSTRACT

Natural gas pipelines could be an important pathway to transport gaseous hydrogen (GH2) as a cleaner alternative to fossil fuels. However, a comprehensive understanding of hydrogen-assisted fatigue and fracture resistance in pipeline steels is needed, including an assessment of the diverse microstructures present in natural gas infrastructure. In thus study, we focus on modern steel pipe and consider both welded pipe and seamless pipe. In-situ fatigue crack growth (FCG) and fracture tests were conducted on compact tension samples extracted from the base metal, seam-weld, and heat affected zone of an X70 pipe steel in high-purity GH2 (210 bar pressure). Additionally, a seamless X65 pipeline microstructure (with comparable strength) was evaluated to compare the different microstructure of seamless pipe. The different microstructures had comparable FCG rates in GH2, with crack growth rates up to 30 times faster in hydrogen compared to air. In contrast, the fracture resistance in GH2 depended on the characteristics of the microstructure varying in the range of approximately 80 to 110 MPa$\sqrt{m}$.

## INTRODUCTION

To reduce global carbon emissions, gaseous hydrogen (GH2) is widely being considered as a low carbon alternative energy carrier for the rising global energy demands. Existing natural gas pipeline network or new dedicated hydrogen pipelines can be a cost-effective medium for transporting GH2 from the site of production to the place of consumption [1]. However, ferritic pipeline steels experience a reduction in toughness and ductility in the presence of GH2 [2-4]. To ensure safe and reliable transport of GH2 through the pipeline network, we must evaluate the structural performance, particularly the fatigue crack growth and fracture behavior of pipeline steels in GH2 environment.

Numerous studies have investigated the fatigue and fracture response of pipeline steels in GH2 environment focusing on the effect of materials parameters like strength, microstructure, environment and test variables [5-8]. Hydrogen assisted fatigue crack growth (HAFCG) rates are accelerated in the presence of GH2 at pressures below 1 bar [9]. The acceleration in HAFCG rates depend on the GH2 pressure and the load-ratio of fatigue cycling, and is typically independent of the strength and microstructure of the steel [6,8]. Pipeline steels also show a substantial reduction in fracture resistance in GH2, even at low pressures [5,7-10]. Unlike HAFCG rates, the fracture resistance of the steel in GH2 is sensitive to the microstructure and more specifically the strength of the steel. Higher strength steels have lower fracture resistance in GH2 [8,11]. Microstructural constituents, such as martensite, are suggested to be detrimental for fracture behavior in GH2 [12].

Pipeline sections are typically manufactured using steel plates that are bent into tubes and then welded along the seam. Welds and their heat affected zone (HAZ) regions can be particularly complicated due to microstructural heterogeneities, presence of residual stresses and the possibility of macroscopic defects [11]. During service, cracks can initiate in or near the weld region and grow through the weld or HAZ microstructure. Therefore, an investigation into the fatigue and fracture response of weld and HAZ microstructures in comparison with the base metal microstructure in GH2 environment is warranted. A few studies have looked at the HAFCG behavior of welds and HAZs, where it was observed that weld and HAZ microstructures largely behave similar to the base metal [13-15]. Ronevich and Somerday [14] reported that the girth weld had higher and HAZ region had lower HAFCG rates (at low $\Delta K$) compared to the base metal of an X65 steel. Contrarily, Drexler *et. al.* [15] showed that the HAFCG rates in the HAZ regions of both seam and girth welds in a vintage X52 pipe were higher than the base metal of

that pipe. Morro et. al. [13] reported insignificant differences in the HAFCG rates of base metal (BM), weld and HAZ microstructures, further adding to the ambiguity of the results. Ronevich *et. al.* [11] investigated fracture resistance of a broad variety of welds in modern steels and found that the welds do not specifically show a lower fracture resistance than the respective base metal (and similar strength), and higher strength welds have lower fracture resistance. However, the influence of strength and microstructure has not been decoupled in the context of fracture resistance in GH2.

The objective of this study is to evaluate and compare hydrogen assisted fatigue and fracture response of the different microstructures present in modern X70 seam-welded, viz. base metal, fusion zone (FZ - weld) and the heat affected zone (HAZ). Additionally, fatigue and fracture behavior of a modern X65 seamless pipe is also investigated and compared with that of a welded pipe. In-situ fatigue and fracture tests were performed in a high-purity GH2 environment using fracture mechanics based samples extracted from the BM, FZ and HAZ of modern X65/X70 pipeline steels. The trends in HAFCG rates and fracture resistance in GH2 are presented in this article.

## EXPERIMENTAL METHODS

### Materials

In this study, fatigue and fracture performance of two modern pipeline materials were evaluated in gaseous hydrogen at a pressure of 210 bar; these two materials are designated as E21 and D20 for simplicity and consistency with other reporting. The E21 pipeline was fabricated in 2021 and contains a seam weld produced by double submerged arc welding (DSAW). The D20 pipeline is a seamless (SMLS) pipe that was fabricated in 2020. The material chemistry complies with API 5L [16], ISO 3183 [17] and DNV-ST-F101 [18] standards, with additional requirements as per ASME B31.12 [28]. Table 1 shows the dimensions and chemical composition of the two pipeline materials

Table 1. Details of the Pipeline Materials Examined in the Study

| | | | | Dimensions (mm) | | Chemical Composition (wt %) | | | | | | |
|---|---|---|---|---|---|---|---|---|---|---|---|---|
| Material | Grade | Year | Weld | OD | thickness | C | Si | Mn | P | S | Nb | Ti |
| E21 | X70 | 2021 | DSAW | 711 | 17.5 | 0.08 | 0.31 | 1.65 | 0.013 | 0.0008 | 0.031 | 0.015 |
| D20 | X65 | 2020 | SMLS | 355.6 | 19.0 | <0.12 | <0.30 | <1.65 | <0.015 | <0.003 | <0.04 | <0.020 |

Fracture mechanics based compact tension (CT) samples (W = 26.4 mm, B = 12.7 mm) were extracted from the pipeline sections in the C-L orientation such that during fatigue and fracture testing, the load was applied along the circumferential (hoop) direction of the pipe and the crack grew along the longitudinal direction. Side-grooves (12% total reduction) were introduced in the CT samples to promote a through-thickness planar crack front. For the E21 steel, in addition to the sample from the base metal region (CT-BM) of the pipe, samples were extracted from the fusion weld (CT-W) and heat affected zone (CT-HAZ) regions as schematically shown in the Figure 1 (a). The weld and heat affected zone (HAZ) are also indicated in the schematic (the pipeline section is not to scale). Figure 1 (b) shows the dimensions of the CT sample used in this study. For the D20 steel, only the base metal sample was extracted as the D20 pipe is seamless.

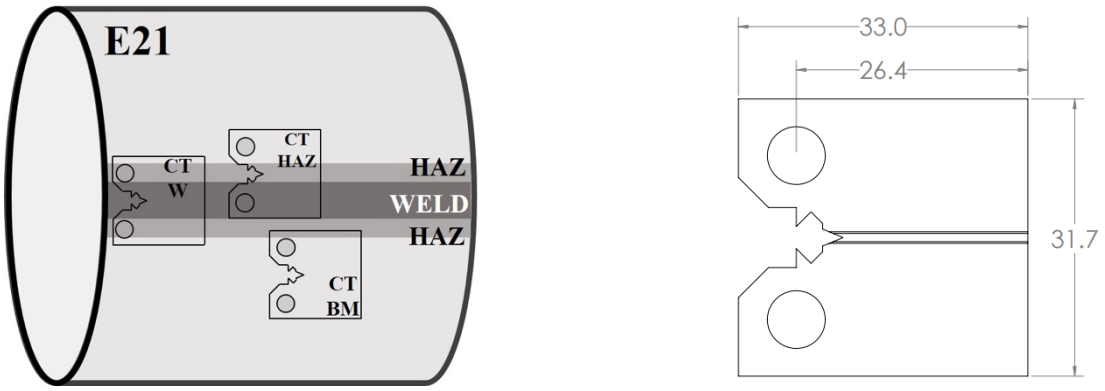


Figure 1. (a) Schematic of specimen extraction location and orientation in the E21 pipeline section. (b) dimensions (in mm) of the compact tension (CT) sample tested in this study for both materials

In addition to CT sample, steel coupons were also extracted for microstructural characterization and hardness measurements. Transverse cross-section of the E21 weld region and D20 base metal was mounted in epoxy resin at room temperature, metallographically polished and etched using 2 % nital to reveal the microstructure in the weld region of the pipe. Optical images were recorded for E21 and D20 base metal, as well as the E21 weld and HAZ, using a Keyence VHX100 digital microscope.

Vickers hardness measurements were performed on the mounted and polished transverse cross sections, using a load of 500-gram force and a dwell time of 10 s. For the E21 steel, 40 mm long line-scans (1 mm indent spacing) were performed at three locations, near outer diameter, mid-thickness, and near inner diameter. For the D20 steel, 20 mm long line-scans (1 mm indent spacing) were performed at the same three locations.

**Hydrogen Assisted Fatigue and Fracture Testing**

Testing in gaseous hydrogen was conducted in custom systems for testing in controlled high-pressure environments [19]. These test systems utilize internal force transducers (i.e., force measured within the pressure boundary) and displacement transducers attached to the specimen at the load line. A rigorous (positive pressure) purging process is employed to ensure the test gas is as pure as possible, using high-purity GH2 (99.9999%) for purging and testing. At the conclusion of some tests, the gas is sampled and tested for oxygen and water content at a commercial laboratory. The oxygen content is typically < 1ppm and water content is typically <10 ppm. The source of the oxygen and water impurities is residual gas from purging as well as off-gassing of the soft goods in the system (wire insulation for transducers, O-rings, etc) and adsorbed species on the internal walls of the vessel (especially water).

In this study, fatigue and fracture tests were performed at a GH2 pressure of 210 bar. The testing was implemented using the Fracture Technology Associates (FTA) testing software. Crack length was monitored using the compliance technique and fatigue crack growth (FCG) tests were executed in K-control. Prior to testing in high-pressure GH2, pre-cracking was performed in air using a two-step process. In the first step, the CT sample was subjected to compression-compression precracking for approximately 5000 cycles to develop a tensile residual stress and introduce a uniform crack front. The conditions selected were based on tensile precracking conditions assuming a $K_{app}$ of 19.8 MPa√m and R=0.1 however the loads were negative. In the next pre-cracking step, tension-tension fatigue cycles were performed using a K-decreasing control strategy. During the tension pre-cracking in air, the fatigue crack grew by approximately 2.5 mm (final a/W = 0.29) as the $K_{max}$ decreased from 19.8 MPa√m to 13.2 MPa√m (constant K-gradient: C = -0.35 $mm^{-1}$). After pre-cracking in air, FCG measurements were performed in accordance with ASTM E647 [20] in the GH2 environment. Multiple K-controlled FCG segments (constant C-gradients of +0.24 and -0.24 $mm^{-1}$ for K-increasing and K-decreasing respectively) were implemented with different load ratios using the FTA fatigue testing software resulting in total fatigue crack extension in GH2 of approximately 10 mm (to a/W = 0.65-0.7). It was ensured that during the fatigue cycling, $K_{max}$ was less than 40 MPa√m and the final $K_{max}$ at the end of the fatigue test was less than 20 MPa√m. The details of testing methodology are described in ref.[7].

At the conclusion of FCG test in GH2, a rising displacement fracture test was implemented on the CT sample in accordance with ASTM 1820 [21]. During the fracture test, a constant current of 2 A was passed through the sample and the voltage was recorded across the crack to determine the crack length using the DCPD technique. Load-line displacement was also recorded as the sample was monotonically loaded in GH2 at a displacement rate of 0.005 mm/min (~0.5 to 1 MPa√m/min). Finally, the CT samples were heat-tinted in a box furnace at 275 C for 45 mins to mark crack extension, cryo-quenched in liquid N2, and fractured by overloading to separate the halves of the specimen. At least two CT samples were tested for each condition.

**Fatigue and Fracture Data Analysis**

Crack extension values were measured from the heat-tinted fractured halves of the CT samples. Measured crack lengths were then used to correct the calculated crack-length data (using compliance technique) and the HAFCG rates (da/dN) were determined by fitting a 7-point-polynomial over the crack-length versus the applied ΔK data using the FTA fatigue analysis software (based on ASTM 647 methods). Elastic plastic fracture mechanics (EPFM) analysis was performed to construct the crack growth resistance curves (J-R) curves for the different materials as described in ASTM 1820 [21]. The fracture resistance in GH2, $K_{JQH}$, was then determined from the J-value at the intersection of the 0.2 mm offset construction line and the J-R curve ($J_{QH}$) using the equation –

$$K_J = \frac{\sqrt{EJ}}{\sqrt{1-\nu^2}}$$

where E is the Young's modulus (207 GPa) and ν is the Poisson's ratio (0.3). In these tests, the geometrical constraints of the specimen are satisfied, such that $J_{QH}$ can be qualified as a specimen-independent measure of the fracture resistance according to ASTM E1820. However, the $J_{QH}$ nomenclature is used to emphasize the observation of non-uniform crack fronts in most cases.

## RESULTS AND DISCUSSION

### Microstructural Characterization

Figure 2 (a) shows an image of the etched cross-section of weld region of the E21 pipe. The fusion zone in the center of the image contains two different melt-pools comprising of columnar grains (region within the blue dotted lines). During the second welding pass, a part of the previous melt-pool experienced re-heating without melting, and likely has a different microstructure from the original solidification microstructure. The narrow region adjacent to the melt-pools, where the material experienced re-heating but not melting during the welding process, is labelled as the heat affected zone (HAZ – region within the pink dotted lines). Finally, the region away from the fusion zone is labelled as the pipeline base material (BM) where the microstructure is unaffected by the welding process.

Three line-scans of hardness indents, near the outer-diameter (1 mm below the surface), middle section (center) and inner-diameter (1 mm above the surface) of the pipe are shown in Figure 2 (a). The measured Vickers hardness along these line scans is presented in Figure 2 (b). The position zero on y-axis nominally represents the center of the FZ of the E21 weld. The edges of the hardness dataset correspond to indents in the BM region, while the transition zone between the FZ and BM indents (characterized the steep gradient in hardness) represents the hardness measurements in the HAZ region. The location of the HAZ varies due to the double-V shape of the FZ. The average Vickers hardness value of in BM, FZ and HAZ is 197.6 ± 5.5 $HV_{0.5}$ (50 indents), 216.7 ± 5.3 $HV_{0.5}$ (52 indents), and 184.4 ± 9.4 $HV_{0.5}$ (18 indents) respectively. The FZ of the weld has higher hardness as compared to the BM, whereas the HAZ region has a lower average hardness than both FZ and BM regions. Due to the microstructural gradients in the HAZ, the standard deviation of the HAZ hardness is approximately twice as large as the standard deviation of the hardness in the other two regions.

Figure 2 (c) and (d) show respectively, an etched cross section of D20 seamless pipe and the hardness line scans 1 mm below the OD, at the mid-thickness and 1 mm above the ID of the pipe. In the absence of a weld, the entire section represents the base material with nominally uniform microstructure. Hardness gradients exist across the pipe wall: higher hardness near the surfaces and lower hardness in the middle. On an average, the hardness of at the mid-thickness (195 ± 3.8 HV) is approximately 16 HV lower than near the outer surface (211.4 ± 4.2) and 30 HV lower than near the inner surface (224.5 ± 8.1 HV). Considering all the indents together (60 indents), the average Vickers hardness of D20 base material is 210.3 ± 13.4 HV. The highest measured hardness was 238 HV while the lowest hardness was 189 HV. This comparatively high standard deviation of hardness can be attributed to subtle microstructural gradients through the wall of the pipe, which is also reflected in the apparent hardness gradients through the wall, likely resulting from water quenching during manufacture of the pipe.

Figure 3 (a) and (b) show the etched back-face of CT samples extracted from the FZ and HAZ respectively. The crack-plane of the E21-FZ sample (blue dashed line) lies within the FZ along the columnar and equiaxed ferrite grains. For the E21-HAZ sample, only a part of the crack-plane (pink dashed line) lies along the HAZ region, while a significant part of the crack-plane lies in the base metal region. Due to the heterogeneous microstructures in the weld and HAZ, extracting representative samples for testing and interpreting the results is particularly challenging. For instance, the crack-plane in the E21-HAZ sample also passes through the base metal microstructure. In the literature, several studies investigate simulated HAZ microstructures (through heat treatments) to navigate the problem of microstructural heterogeneities [22,23]. Alternatively, some researchers have used smaller samples and other geometries like single edge crack tensile sample to target specific locations of the weld and HAZ regions in the sample [14]. However, in both the above-mentioned approaches, simulated microstructures or smaller geometries (including CT samples), the residual stresses are relieved and re-distributed, and therefore, the samples do not accurately capture or represent the structural response of the pipe during service.

Figure 4 (a-c) show high-magnification optical images of E21-BM, FZ, and HAZ, respectively. The BM exhibits a banded ferrite (light regions) – pearlite (dark regions) microstructure with approximately 15 % pearlite (Figure 4 (a)). The banded microstructure results from the hot rolling step during the manufacturing of the steel plates used to fabricate the welded pipe. The weld microstructure (Figure 4 (b)) predominantly contains fine acicular and some allotriomorphic ferrite along the prior austenite grain boundaries. Additionally, small amounts of non-equilibrium austenite decomposition products may be present in the weld microstructure. Depending on the distance from the fusion line, regions of HAZ can experience high reheating temperatures causing grain coarsening. The HAZ microstructure (Figure 4(c)) was imaged in the vicinity of the weld melt-pool (top-right region of the image is the weld) and contains a mixture of coarse ferrite grains as well as non-equilibrium phases formed during the reheating and cooling cycle of the welding process. The nature of the non-equilibrium phase is not discernible with the optical micrographs, but different researchers have previously reported the presence of fine pearlite, bainite or martensite-austenite constituents in the coarse grained HAZ of submerged arc welds in pipe[24,25]. Figure 4(d) shows the base material microstructure of D20 steel from the mid-thickness region comprised of a mixture of tempered upper and lower bainite. Cementite is present along the boundaries of the bainitic substructure. The microstructure near the ID was pre-dominantly lower bainite and near the OD was a mixture of upper and lower bainite (not shown here).

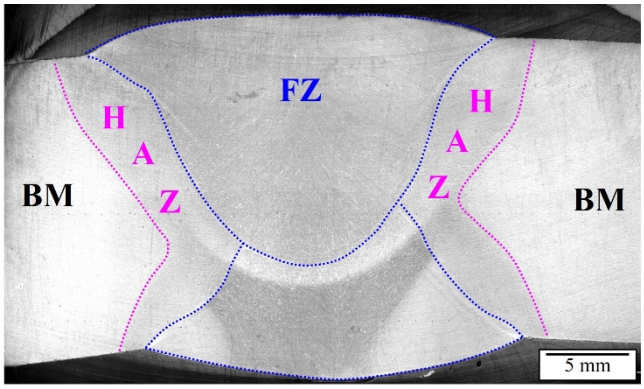


(a)

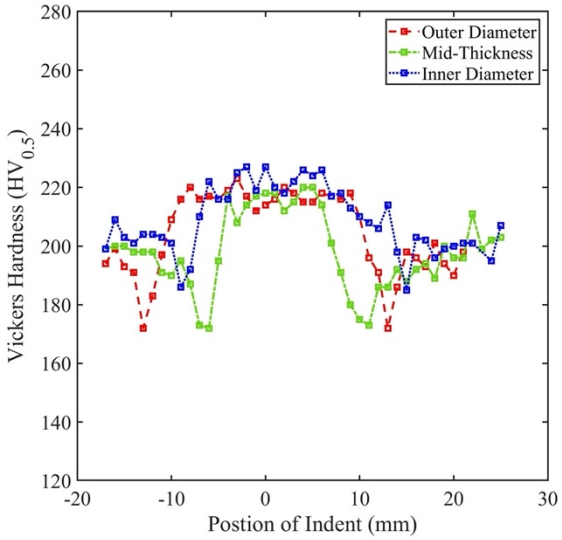


(b)

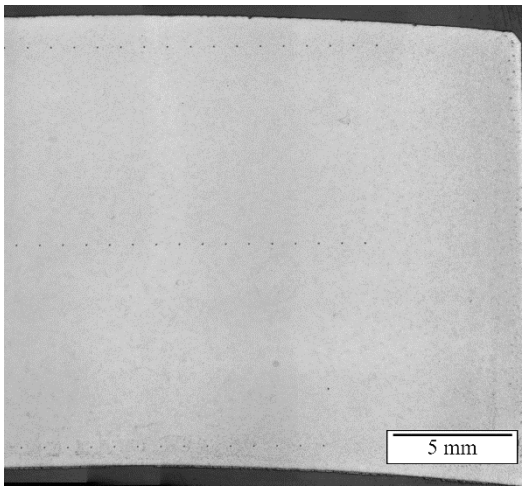


(c)

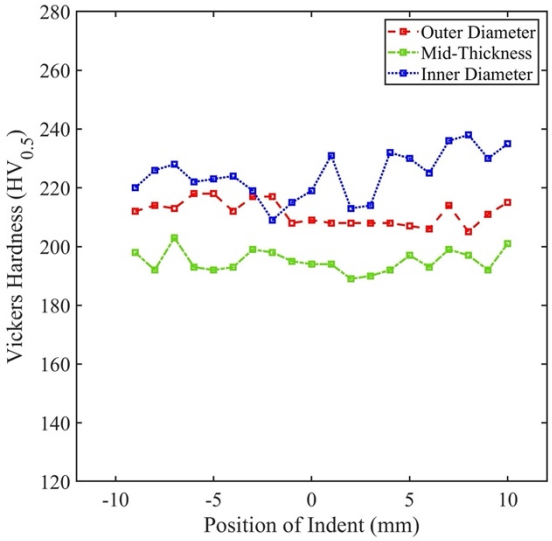


(d)

Figure 2. Seam weld cross section from the E21 pipe: (a) low magnification optical image; and (b) line scans of Vickers microhardness across the weld seam near the OD, at the mid-thickness, near the ID of the pipe. Through-wall section of the D20 seamless pipe: (c) low magnification optical image and (d) line scans of the microhardness near the OD, at the mid-thickness, and near the ID of the D20 pipe.

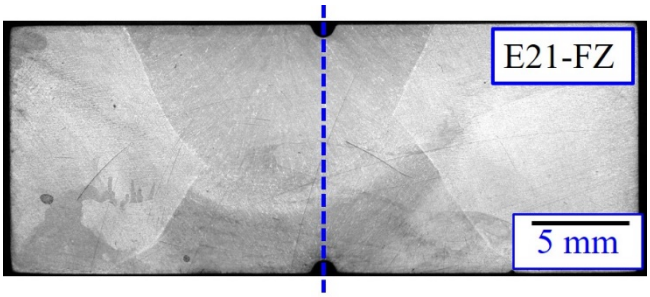


(a)

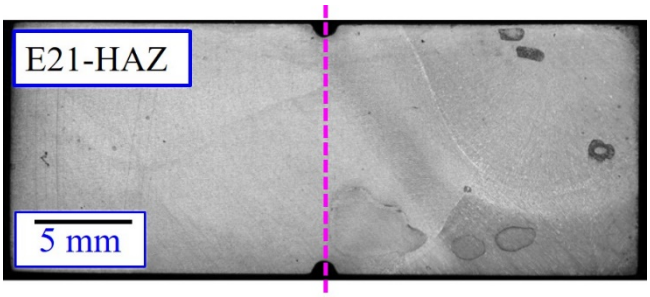


(b)

Figure 3. Polished and etched back face of CT samples extracted from the FZ and HAZ regions of the E21 seam weld.

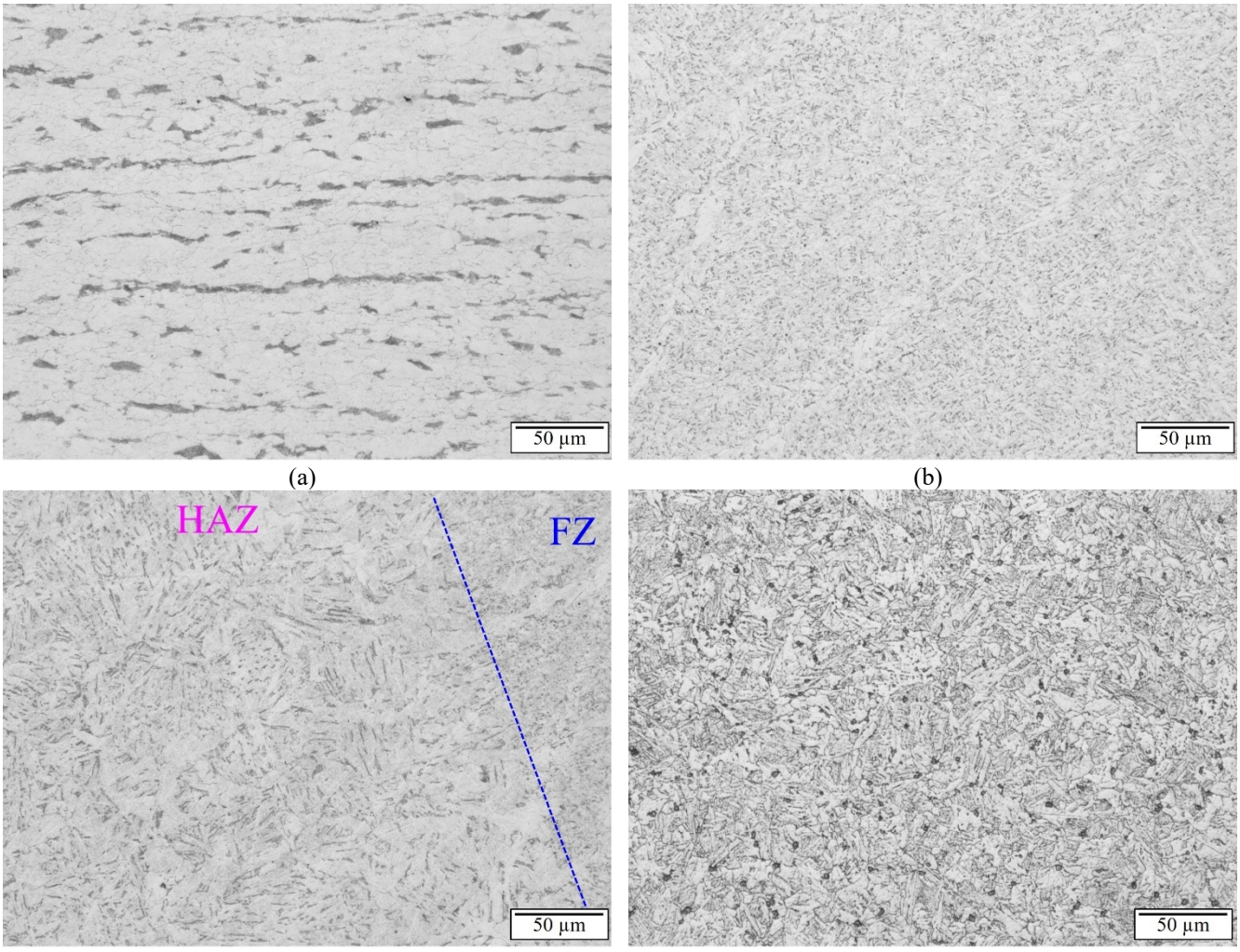

Figure 4. Light optical micrographs of (a) E21-BM, (b) E21-FZ, (c) E21-HAZ, and (d) D20-BM.

**Hydrogen Assisted Fatigue Crack Growth**

Hydrogen-assisted fracture crack growth rates are shown in the typical fashion, as a function of the stress intensity factor range (ΔK) in Figure 5. HAFCG for load ratio (R) of 0.5 and a frequency of 1 Hz is presented in Figure 5 (a). The solid black line shows the generic power-law relationship for FCG in line pipe steels from API 579 equation 9F.5.3.3(b) (this relationship does not depend on R or frequency) [26]. The measured HAFCG rates for all the microstructures (E21-BM, -FZ, -HAZ and D20-BM) are substantially higher than the prediction in air by a factor of 4 to 30 times (low to high ΔK). The dotted line in Figure 5 (a) represents the pressure- and R-dependent master design curves (MDC) at R = 0.5 and GH2 pressure of 210 bar, as adopted in ASME B31 Code Case 220 and described by San Marchi *et. al.* [27]. All tested microstructures show very similar HAFCG rates that nominally follow the MDC predictions. The difference in the HAFCG rates between the microstructures is less than a factor of two, which is of the order of test-to-test variation in replicate testing (of the same material/microstructure).

The HAFCG data in Figure 5 (b) corresponds to fatigue cycling at R = 0.7 and a frequency of 5 Hz. Since the $K_{max}$ during testing was limited to below 40 MPa√m, the probed ΔK range for R = 0.7 is lower than that for R = 0.5. The solid black line shows the predicted FCG rates in air as per the API 579 document while the dashed line shows the MDC prediction for HAFCG rates at a load ratio of 0.7 in GH2 pressure of 210 bar. As for the R = 0.5 data, the different microstructures exhibit very similar HAFCG rate and closely follow the MDC predictions for R = 0.7 (the higher frequency was used to accommodate the lower FCG rate).

Despite significantly different processing histories and microstructure, the HAFCG rates are nearly identical for the E21-BM and D20-BM samples. This observation is consistent with previous studies investigating the HAFCG behavior of pipeline steels and pressure vessel steels with different microstructures [5], and strength level (API grades) [8]. However, upon closer inspection of the measured HAFCG in E21-BM, FZ and HAZ tests, it is observed that for both load ratios, the HAFCG rates

of the FZ are slightly higher than the BM and the HAZ displays slightly lower HAFCG rate than the BM. This observation is consistent with a previous result from Ronevich *et al.* [14] where the difference in HAFCG rates was attributed to external factors like crack closure and the presence of residual stresses in the weld region. In the regions with tensile residual stress, both the effective $K_{max}$ and $K_{min}$ are higher than the applied $K_{max}$ and $K_{min}$, resulting in a higher effective load ratio, which results in higher da/dN for a given ΔK. Similarly, in regions of compressive residual stress, the effective load ratio is lower than the applied load ratio. Thus, the presence of residual stresses in the weld region of E21 steel may provide an explanation for the small differences in the observed HAFCG rates. The relative HAFCG rates of BM, FZ and HAZ microstructures observed in this study may not always be true for all welded pipelines. Drexler *et. al.* [15] argue that whether the FZ or HAZ will show higher or lower HAFCG rates than BM can depend on the microstructure, welding technique and relative strength of the weld with respect to the BM. In general, however, HAFCG is relatively insensitive to microstructure and strength in the absence of residual stress and significant microstructural non-uniformity (such as banded pearlite [14]).

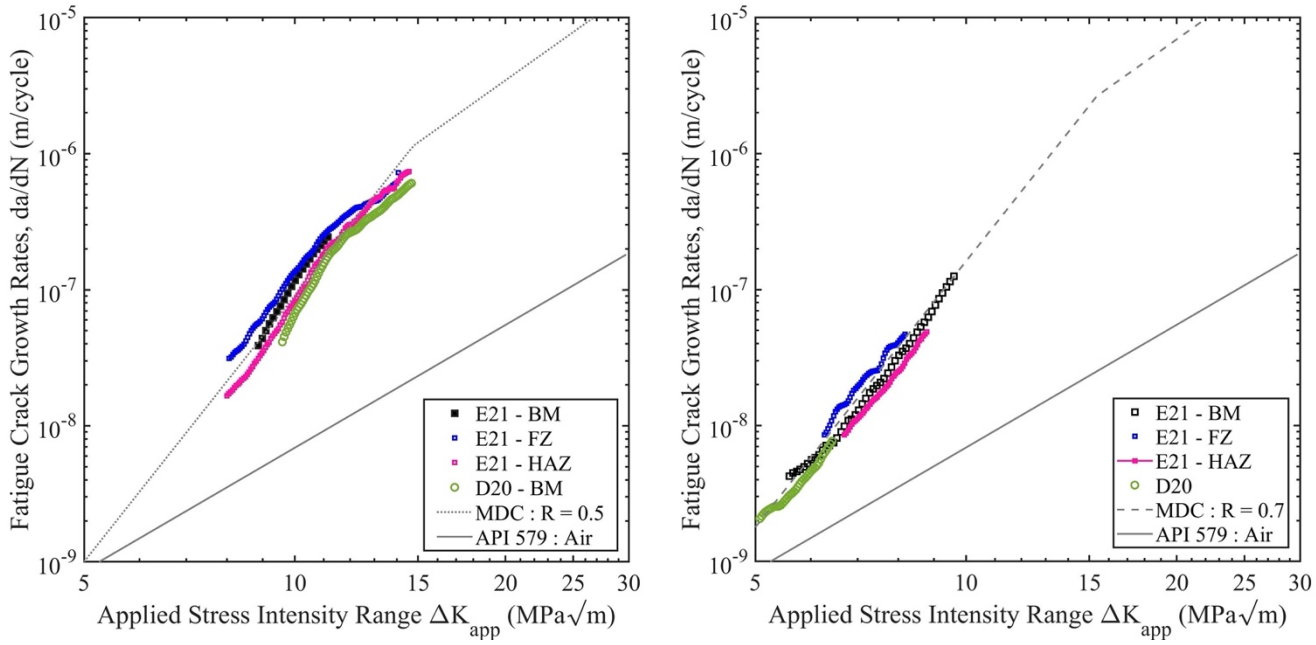


(a) R = 0.5 (b) R = 0.7

Figure 5. Hydrogen assisted fatigue crack growth rates in E21-BM, FZ, HAZ and D20-BM microstructures tested in GH2 environment at a pressure of 210 bar: (a) load ratio of 0.5 and cycling frequency of 1 Hz, and (b) load ratio of 0.7 and cycling frequency of 5 Hz.

**Hydrogen Assisted Fracture**

The hydrogen-assisted fracture resistance ($K_{JQH}$) is shown in Figure 6 (a) for the materials tested in GH2. The cyan bars represent an average of $K_{JQH}$ from two measurements, while the blue squares show the individual measurements. Average Vickers hardness ($HV_{0.5}$) is also included in the figure for each material. As shown in Figure 2(b), the hardness of the BM and FZ is consistent at the three measured locations through the thickness, so we anticipate a relatively uniform hardness across the crack front for fracture tests in these locations (E21-BM and E21-FZ respectively). The hardness of E21-HAZ is variable and the HAZ is not aligned with crack front; as shown in Figure 7(c), a large part of the crack plane lies in the BM region. Therefore, we may anticipate more variation in the local hardness along the crack front of the HAZ samples compared to the BM and FZ of E21. Similarly, the through-thickness hardness of the D20 pipe is non-uniform (Figure 2(d)), thus the hardness likely varies along the crack front. However, since the D20 samples were extracted from the middle of the pipe wall, the average hardness along the crack plane will be biased toward the hardness at the middle and lower than the cumulative average of 210 HV.

The fracture resistance (in GH2 at a pressure of 210 bar) of all the tested samples was in the range of 80 to 110 MPa√m, higher than the 55 MPa√m requirement for hydrogen pipelines as per ASME B31.12 [28]. Unlike the microstructure-independent HAFCG behavior, the fracture resistance in GH2 is different for each material and microstructure. The E21-FZ sample with fine ferritic microstructure has a higher fracture resistance than the E21-BM microstructure of ferrite and pearlite both. In general, the materials with lower hardness show higher fracture resistance [11], however, other factors also contribute to fracture resistance. Pearlite, for example, is a hard, brittle phase that can lower the fracture resistance. The lower hardness of the E21-BM may be offset by the presence of pearlite, leading to the lower observed fracture resistance compared to E21-FZ with comparatively higher hardness. The two measurements of $K_{JQH}$ for the E21-HAZ condition are substantially different, likely due to the differences in location of the crack plane with respect to the weld boundary. The lower measured value for the

E21-HAZ condition is similar to the fracture resistance of E21-BM material, likely due to the crack front propagating mostly in the ferrite/pearlite BM (Figure 7(c)) with a minority portion of the crack front actually in the ferritic HAZ microstructure. The second measured value for the E21-HAZ is higher, perhaps reflecting a greater proportion of the crack front in the ferritic HAZ microstructure. Similar to the E21-FZ microstructure, the D20-BM microstructure also does not have pearlite and shows relatively high fracture resistance in GH2, comparable to that of the E21-FZ microstructure. The finer, relatively more uniform bainitic microstructure of the D20 steel provides improved hydrogen-assisted fracture resistance as compared to the coarser banded ferrite pearlite microstructure of the E21 steel.

The J-R curves (J-integral versus crack extension) for the different microstructural conditions (two samples each – solid and dashed lines) are shown in Figure 6 (b). All the materials exhibit a rising R curve behavior. The E21-BM and E21-HAZ materials show slightly lower fracture initiation resistance (J at crack initiation represented by the sharp inflection of the J-R curve near zero crack extension) than the other materials The slope of the J-R curve, indicating the resistance to fracture propagation, is significantly different for the different microstructures. E21-BM and E21-HAZ display a shallower slope of the J-R curve as compared to the E21-FZ and D20-BM samples, thus lower resistance to crack propagation as well as lower resistance to crack initiation. These observations suggest that the presence of pearlite in the crack plane likely influences both fracture initiation and the fracture propagation process in GH2 environment. Both E21-FZ and D20-BM materials have comparable J-R curves in terms of both fracture initiation and the slope of the J-R curve during the initial stage of crack extension.

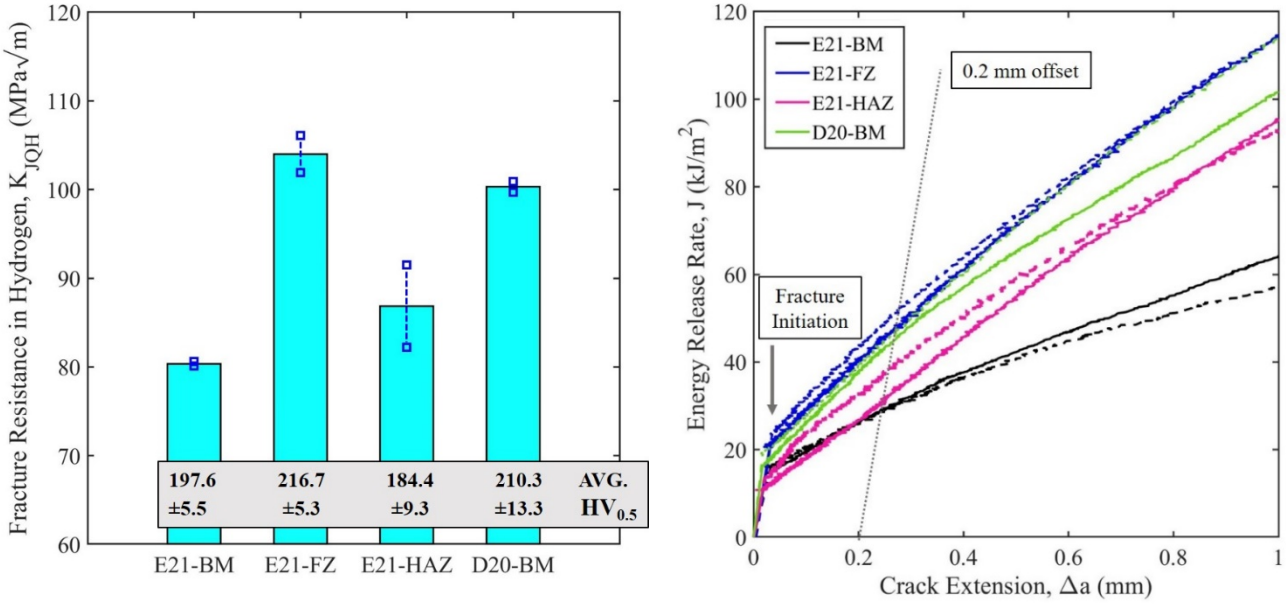


(a) (b)

Figure 6. Hydrogen assisted fracture resistance of E21-BM/FZ/HAZ and D20-BM microstructures (a) the KJQH values, and (b) the corresponding J-R curves.

**Fracture Surface Analysis**

Figures 7 (a-d) show a fractured half of a CT sample for each of the tested materials: E21-BM, E21-FZ, E21-HAZ and D20-BM, respectively. The direction of fatigue crack and fracture propagation is from top to bottom in all the images. Due to heat-tinting, four distinct regions with different color (shade) can be observed on each of the fracture surfaces. The light-blue/purple region at the top represents crack extension during the fatigue pre-cracking in laboratory air. The lighter region below the pre-crack represents crack extension during HAFCG in the GH2 environment. The subsequent darker and thin region show fracture propagation during the rising displacement fracture test in the GH2 environment. Finally, the lightest region (no heat-tinting) at the bottom of the sample resulted from overloading after cryo-quenching in LN2. The above mentioned regions are labelled on the fracture surface of E21-BM sample in Figure 7 (a).

The shapes of the fatigue crack fronts are visibly different for all conditions. The base metal of the ferrite-pearlite pipe (E21-BM in the Figure 7 (a)) has a planar fatigue crack front both in the air pre-crack and HAFCG region of the fracture surface suggesting that the base metal microstructure is uniform through the thickness of the sample. In Figure 7 (b) and (c), the FZ and HAZ samples show a concave and a convex fatigue crack front respectively in both air and GH2. In the FZ sample, finer grains are present in the center of the specimen while the edges of the sample have larger columnar grains. In the HAZ sample, a part of the crack grows through a coarse ferritic HAZ microstructure, while the rest of the crack intercepts the ferrite/pearlite

base metal microstructure. The approximate location of the BM and HAZ microstructure in the crack plane of E21-HAZ sample is highlighted in Figure 7(c)). Further, residual stresses are known to be present in welds (although no effort was made to quantify residual stress in this weld), which can alter the effective stress intensity ($K_{max}$ and $K_{min}$) at the crack tip and the subsequent local HAFCG rate [29]. Thus, a combination of microstructural gradient, and the local residual stresses play a role in the observed shape of the fatigue crack front in E21-FZ and HAZ samples. For the D20-BM sample in Figure 7 (d), the crack front is slightly concave, likely due to the microstructural gradient through the thickness of the sample as evidenced by the differences in Vickers microhardness values near the OD, ID and in the mid-thickness line scans (Figure 2(d)).

The fracture extension follows the fatigue crack front for E21-FZ, E21-HAZ and D20-BM samples. The E21-BM and the E21-HAZ fracture regions show micro-delaminations, which point to non-uniform microstructure with interfaces that are susceptible to debonding. The banded ferrite pearlite microstructure in the fracture plane of both the E21-BM and HAZ samples may be the origin of the observed micro-delaminations. The fracture surfaces of the E21-FZ and D20-BM that have higher fracture resistance in GH2 do not show delamination presumably due to their fine relatively uniform microstructures. Notably, in the case of E21-BM sample, the shape of the fracture extension does not follow the fatigue crack front due to a large delamination along the center of the sample. This feature is likely associated with centerline segregation, an unavoidable manufacturing defect from the initial continuous casting step of the manufacturing process of plate prior to welding into pipe [30]. Centerline segregation is known to be deleterious for mechanical properties of pipeline steels [30]. Similar delamination was not observed in the D20-BM sample from the SMLS pipe.

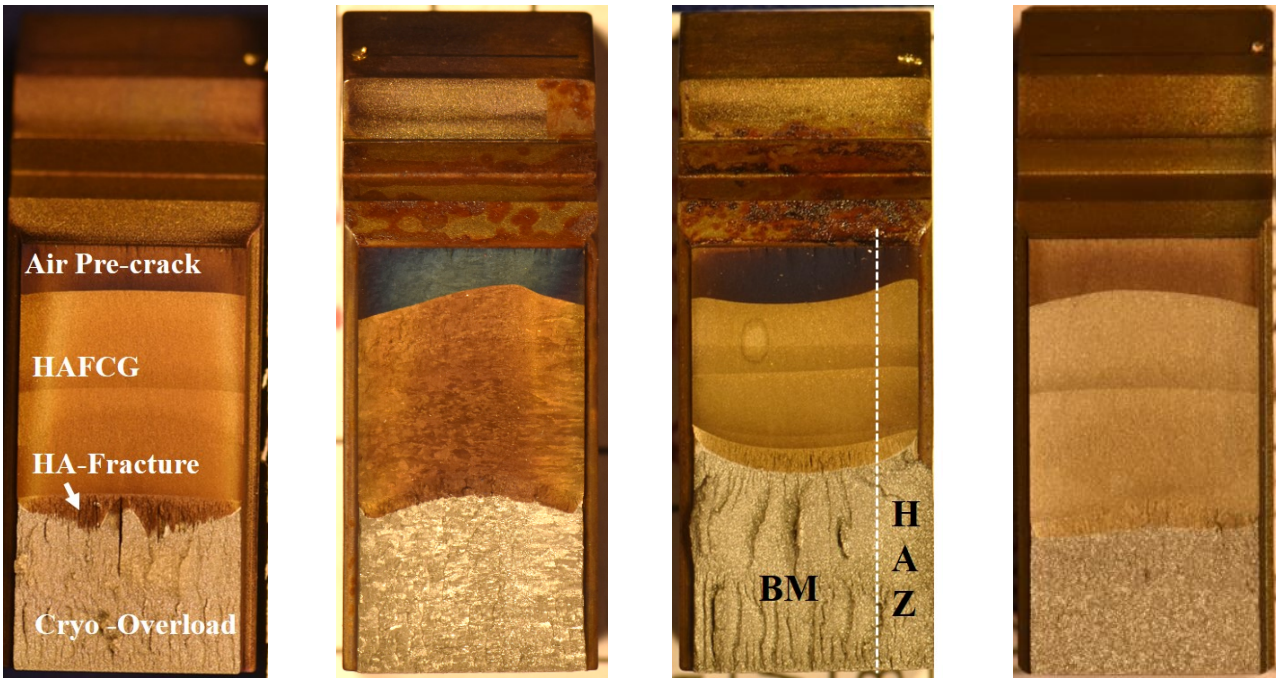


(a) (b) (c) (d)

Figure 7. Heat-tinted fracture surfaces of CT samples of (a) E21-BM, (b) E21-FZ, (c) E21-HAZ, and (d) D20-BM.

## CONCLUSIONS

In this study, HAFCG and hydrogen-assisted fracture of welded (E21) and seamless (D20) pipes were evaluated in gaseous hydrogen at pressure of 210 bar. Fatigue and fracture samples were extracted from the both the base metal and the seam weld of the welded pipe as well as the heat-affected zone (of the seam). Fatigue crack growth was observed to be similar for both pipe steels as well as the fusion zone and heat-affected zone of the seam weld for load ratio of 0.5 and 0.7 respectively. However, the magnitude of fatigue crack growth was up to 30 times greater than expected in air. Additional work on the effect of external factors like the presence of residual stresses would allow better understanding of the HAFCG rates of weld region. Hydrogen-assisted fracture resistance was greatest in the ferritic fusion zone of the welded pipe and the bainitic microstructure of the seamless pipe. Despite lower hardness, the base metal of the ferrite-pearlite pipe material (E21) showed the lowest hydrogen-assisted fracture resistance due to the presence of the hard, brittle pearlitic phase. The samples extracted near the heat-affected zone, consisted mostly of base metal along the crack front with a minority fraction of the lower hardness heat-affected zone, thus fracture of these samples reflected the fracture resistance of the base metal. Quantitatively, the fracture resistance of both materials and all microstructures was significantly lower than anticipated in air but remained between approximately 80 and 110 MPa$\sqrt{m}$ in the high-pressure hydrogen test environment (hydrogen partial pressure of 210 bar).

## ACKNOWLEDGEMENTS

Sandia National Laboratories is a multi-mission laboratory managed and operated by National Technology & Engineering Solutions of Sandia, LLC (NTESS), a wholly owned subsidiary of Honeywell International Inc., for the U.S. Department of Energy's National Nuclear Security Administration (DOE/NNSA) under contract DE-NA0003525. This written work is authored by an employee of NTESS. The employee, not NTESS, owns the right, title and interest in and to the written work and is responsible for its contents. Any subjective views or opinions that might be expressed in the written work do not necessarily represent the views of the U.S. Government. The publisher acknowledges that the U.S. Government retains a non-exclusive, paid-up, irrevocable, world-wide license to publish or reproduce the published form of this written work or allow others to do so, for U.S. Government purposes. The DOE will provide public access to results of federally sponsored research in accordance with the DOE Public Access Plan. This content is based upon work supported by the U.S. Department of Energy's Office of Energy Efficiency and Renewable Energy (EERE) under the Hydrogen and Fuel Cell Technologies Office (HFTO) from the Pipeline Blending CRADA (a HyBlend™ program) under the direction of Mark Richards.

## REFERENCES

1. James R. Fekete, Jeffrey W. Sowards, and Robert L. Amaro. *Economic Impact of Applying High Strength Steels in Hydrogen Gas Pipelines,* International Journal of Hydrogen Energy 40.33 (2015): 10547-10558.
2. Walter R, Chandler WT, *Influence of Gaseous Hydrogen on Metals—Final Report,* Rocketdyne, Canoga Park, CA, National Aeronautics and Space Administration Report NASA-CR124410, 1973.
3. HJ Cialone, JH Holbrook, *Sensitivity of Steels to Degradation in Gaseous Hydrogen. ASTM STP 962—Hydrogen Embrittlement: Prevention and Control,* ASTM International, West Conshohocken, PA, 1988.
4. D Hardie, EA Charles, AH Lopez, *Hydrogen Embrittlement of High Strength Pipeline Steels,* Corrosion Science 48(12):4378–4385, 2006.
5. C San Marchi, B P Somerday, K A Nibur, D G Stalheim, T Boggess, S Jansto, *Fracture and fatigue of commercial grade API pipeline steels in gaseous hydrogen,* In: Proceedings of ASME 2010 pressure vessels & piping division conference; 2010. Bellevue, Washington USA.
6. Nanninga N, Slifka A, Levy Y, C White, *A review of fatigue crack growth for pipeline steels exposed to hydrogen,* Journal of the Research of the National Institute of Standards and Technology, 115, (2010), 437-52,.
7. C San Marchi, J A Ronevich, *Fatigue and Fracture of Pipeline Steels in High-Pressure Hydrogen Gas,* volume 4B of Pressure Vessels and Piping Conference, (2022).
8. M Agnani, J Ronevich, C San Marchi, *Fatigue and Fracture Resistance of Different Line Pipe Grade Steels in Gaseous H2 Environment*, AMPP Conference and Expo, (2024).
9. J A Ronevich, C San Marchi, *Materials Compatibility Concerns for Hydrogen Blended Into Natural Gas,* Pressure Vessels and Piping Conference, (2021).
10. J.J. Hoyos, M. Masoumi, V.F. Pereira, A.P. Tschiptschin, M.T.P. Paes, J.A. Avila, *Influence of Hydrogen on the Microstructure and Fracture Toughness of Friction Stir Welded Plates of API 5L X80 Pipeline Steel,* International Journal of Hydrogen Energy, 44.41 (2019) : 23458-23471.
11. J.A. Ronevich, E.J. Song, B.P. Somerday, C.W. San Marchi, *Hydrogen-Assisted Fracture Resistance of Pipeline Welds in Gaseous Hydrogen,* International Journal of Hydrogen Energy, 46, (2021) pp. 7601- 761.
12. E.V. Chatzidouros, V.J. Papazoglou, T.E. Tsiourva, D.I. Pantelis, *Hydrogen Effect on Fracture Toughness of Pipeline Steel Welds, with In-Situ Hydrogen Charging,* International Journal of Hydrogen Energy, 36 (2011), pp. 12626-12643.
13. I Moro, L Briottet, P Lemoine, O Doyen, G de Dinechin, *Fatigue Crack Growth of a C-Mn Steel and Associated Weld under Hydrogen Pressure,* International Hydrogen Conference, Hydrogen-Materials Interactions (ASME Press, Moran, WY), (2012), pp 309–317.
14. Joseph Allen Ronevich, and Brian P. Somerday, *Assessing Gaseous Hydrogen Assisted Fatigue Crack Growth Susceptibility of Pipeline Steel Weld Fusion Zones and Heat Affected Zones,* Materials Performance and Characterization (2016).
15. E S Drexler, A J Slifka, R L Amaro, J W Sowards, M J Connolly, M L Martin, and D S Lauria, *Fatigue Testing of Pipeline Welds and Heat-Affected Zones in Pressurized Hydrogen Gas,* Journal of Research of the National Institute of Standards and Technology, 124 (2019): 1.

16. API, API Specification 5L, 46th Edition, 2018.
17. ISO, NS-EN ISO 3183: *Petroleum and Natural Gas Industries - Steel Pipe for Pipeline Transportation Systems,* 2020.
18. DNV-ST-F101, *Submarine Pipeline Systems,* 2021.
19. B P Somerday, J A Campbell JA, K L Lee, J A Ronevich, C San Marchi, *Enhancing Safety of Hydrogen Containment Components through Materials Testing under In-Service Conditions,* International Journal of Hydrogen Energy, (2017);42:7314-21.
20. ASTM Standard E647, *Standard Test Method for Measurement of Fatigue Crack Growth Rates,* 2011.
21. E1820-18a *Standard Test Method for Measurement of Fracture Toughness*, ASTM, West Conshohocken, PA, 2018.
22. S Moeinifar, A H Kokabi, H R Madaah Hosseini, *Influence of peak temperature during simulation and real thermal cycles on microstructure and fracture properties of the reheated zones*, Materials & Design 31.6 (2010): 2948-2955.
23. A Lambert-Perlade, A F Gourgues, J Besson, T Sturel, A Pineau, *Mechanisms and Modeling of Cleavage Fracture in Simulated Heat-Affected Zone Microstructures of a High-Strength Low Alloy Steel*, Metallurgical and Materials Transactions A 35 (2004): 1039-1053.
24. S H Hashemi, D Mohammadyani, M Pouranvari, S M Mousavizadeh, *On the Relation of Microstructure and Impact Toughness Characteristics of DSAW Steel of Grade API X70,* Fatigue & Fracture of Engineering Materials & Structures 32.1 (2009): 33-40.
25. A Joarder, S C Saha, A K Ghose, *Study of Submerged Arc Weld Metal and Heat-Affected Zone microstructures of a plain carbon steel, Welding Research Supplement* 22.6 (1991): 141-146.
26. T L Anderson, D A Osage *API 579: a comprehensive fitness-for-service guide*, International Journal of Pressure Vessels and Piping, 77.14-15 (2000): 953-963.
27. C San Marchi, J A Ronevich, P Bortot, Y Wada, J Felbaum, M Rana, *Technical Basis for Master Curve for Fatigue Crack Growth of Ferritic Steels in High-Pressure Gaseous Hydrogen*, ASME Section VIII-3. Proceedings of the ASME 2019 Pressure Vessels & Piping Conference, San Antonio, TX, 2019.
28. ASM B31.12, *Hydrogen Piping and Pipelines,* 2019.
29. J A Ronevich, C R D'Elia, M R Hill, *Fatigue Crack Growth Rates of X100 Steel Welds in High Pressure Hydrogen Gas Considering Residual Stress Effects*, Engineering Fracture Mechanics 194 (2018): 42-51.
30. F Guo, X Wang, W Liu, C Shang, R D K Misra, H Wang, T Zhao, C Peng, *The Influence of Centerline Segregation on the Mechanical Performance and Microstructure of X70 Pipeline Steel,* Steel Research International 89, no. 12 (2018): 1800407.